Reaction front propagation in nanocrystalline Ni/Al composites: a Molecular Dynamics study

O Politano, Florence Baras

Reaction front propagation in nanocrystalline Ni/Al composites: a Molecular Dynamics study

O. Politano[1, a)] and F. Baras[1, b)]

Laboratoire Interdisciplinaire Carnot de Bourgogne,
UMR 6303 CNRS-Université Bourgogne Franche-Comté,
9 Avenue A. Savary, BP 47 870, F-21078 DIJON Cedex,
FRANCE

(Dated: 6 November 2020)

This work focuses on a class of nano-laminated Ni/Al composites fabricated by a rolling-stacking procedure. This method results in nano-laminated composites with a complex structure. Their reactivity was compared with that of reactive multilayer nanofoils with constant bilayer thickness. Typical samples are composed of randomly distributed grains of Ni and Al. The self-propagating reactive front presents peculiarities that are directly related to the initial microstructure. The combustion mode is unsteady, with shifts in velocity. The temperature profile is characterized by broad combustion and post-combustion zones. The instantaneous shape of the front is tortuous, with the appearance of hot spots correlated with the underlying grain configuration. Local dynamics was studied in order to detect all the elemental processes occurring at nanoscale that trigger propagation: melting of Al, coarsening of Al grains, progressive exothermic dissolution mixing, heterogeneous nucleation and growth of the intermetallic phase, *B*2-NiAl. The role of the complex initial microstructure was clearly demonstrated.

[a)]Electronic mail: olivier.politano@u-bourgogne.fr
[b)]Electronic mail: florence.baras@u-bourgogne.fr

I. INTRODUCTION

Nickel/Aluminum nano-composites are reactive materials able to deliver a large amount of localized heat in a very short time. They are commonly used as chemical energy storage in microscale energetic devices because of their high-energy density. The two main types are nano-composite particles (RCPs) and reactive multilayer nanofoils (RMNFs). Their unique properties make Ni/Al nano-composites good candidates for various applications, such as the controlled neutralization of biological hazards[1], miniaturized heat sources for micro-/nano-scale propulsion systems, micro-electro-pyrotechnic igniters[2], and thermal batteries. In addition, Ni/Al nano-composites are widely used in joining applications to bond heat-sensitive materials[3], carbon materials, metals, and ceramic-metal pairs[4]. Reactive multilayer nanofoils contain alternating Ni and Al layers, with bilayer thickness ranging from a few to a hundred nanometers. After initiation at a discrete point, a rapid self-propagating reaction develops without any further supply of energy, and the temperature sharply increases in a very short time. Nickel/Aluminum is certainly one of the most studied RMNF systems[5,6].

There are several preparation methods for RMNFs[7]. Magnetron sputtering is a very powerful technique for the production of metallic nanofoils with thousands of alternating layers of constant thickness[8,9]. The main drawbacks are its high cost and relatively slow production speed. Multiple rolling, based on a multiple rolling-stacking procedure, is a less expensive alternative method to the deposition method. First, the thin metallic films are packed, pressed, and annealed. Next the film is rolled to reduce its thickness, and then folded. This process may be repeated many times. Cold-rolled aluminum-nickel multilayers (with an excess of Al) have been studied by Sieber *et al*[10]. The rolling procedure results in a drastic decrease in thickness of the elemental foils and a reduction in grain size. In comparison with RMNFs obtained by sputtering, layering develops in a chaotic manner during cold rolling. Self-propagating reactions have been studied in cold-rolled Ni/Al (equimolar) laminate foils[11]. The reaction front image shows a complex structure, with nucleating bands moving perpendicular to the main propaga-

tion direction. Velocity and maximum temperature were found to vary in relation to processing conditions but not to volume average bilayer thickness. Front characteristics could not be predicted effectively, at least with current analytical models.

Over the past decades, reactivity and SHS (Self-propagating High-temperature Synthesis) in Ni/Al nanofoils have been largely investigated (for a review, see[12] and references therein). Modeling approaches are mainly restricted to the case of nanofoils with constant thickness and perfect crystalline lattice structure. Recent studies have explored the influence of defects on combustion in such Ni/Al nanolaminates. Increasing vacancy concentration has been found to increase both reaction rates and temperature peaks[13]. The role of grain size and columnar grain boundaries, such as those observed in RMNFs fabricated by physical vapor deposition (PVD) techniques, has also been investigated[14,15]. Another important issue concerns RMNFs fabricated by mechanical methods such as cold-rolling. The aim of this work is to investigate the reactivity of cold-rolled nanofoils (CR-nanofoils). The very possibility of a self-propagating reaction will be investigated. Combustion characteristics will then be considered as a function of the typical microstructure of CR-nanofoils. The intrinsic microstructure reflects the intermixing at nanoscale induced by the process itself. For instance, Sieber *et al.*[10] reported that, after 70 folding and rolling cycles, the Al and Ni grains are randomly mixed, with a grain size of about 30 nm. The control of the reaction requires a good understanding of the mechanisms involved. In this respect, the Molecular Dynamics approach allows us to capture the basic mechanisms driving the SHS reaction such as diffusion, creation of defects, local ordering/disordering, phase transformations, and dissolution at interfaces[16–21].

II. SIMULATION DETAILS

Molecular dynamics (MD) simulations were performed using Large-scale Atomic/Molecular Massively Parallel Simulator (LAMMPS) code[22], and the Embedded Atom Method

(EAM) potential developed by Mishin et *al.* for the Ni-Al system[23]. Based on accurate potentials for the two pure elements, this method reliably describes the physical properties of binary compounds, and the relative stability of intermetallic phases across the Ni-Al phase diagram[24]. This transferability is important for studies of reactive Ni-Al nanometric multilayers where phase transformations occur[12].

The phenomenon of wave propagation studied here requires a specifically designed elongated sample, as used in our previous approaches on RMNFs[12,17,21]. In the x-direction, the box ranges in size from 0.33 to 0.51 μm; in the y-direction, the size is between 17 nm and 25 nm; in the z-direction, the size is set at 1.4 nm. Samples were subjected to periodic boundary conditions in the y- and z-directions, while shrink-wrapped boundaries were imposed in the x-direction. Shrink-wrapped boundary correspond to a free face that allows the simulation box to encompass the atoms in that dimension.

Two different systems were constructed to compare the properties of CR-nanofoils and RMNFs. The first system mimics the typical structure of CR-nanofoils (see Fig. 1a). Voronoï tesselation creates a polycristalline structure[25] filled with <001> oriented columnar grains, randomly rotated around the z-direction. These polycrystalline samples were composed of 480 grains with a radius of $\sim$ 3.5 nm, 320 grains with a radius of $\sim$ 5 nm, and 240 grains with a radius of $\sim$ 7.5 nm. System characteristics and grain-size distribution are given in Table I and Fig.2. The second system is a layered Ni-Al nanofoil composed of two bilayers, each made up of one slice of Ni and one slice of Al, as previously presented in the literature[12,17,21]. The stoichiometric ratio between Ni and Al is close to the equiatomic ratio ($N_{\mathrm{Ni}}/N_{\mathrm{Al}} = 1.005$). The bilayer thicknesses, H, were designed to be very similar in size to the grain diameters of the CR-samples.

The systems were created and relaxed at 300 K with a fixed number of atoms, pressure, and temperature (NPT ensemble), using the Parrinello-Rahman barostat for 0.4 ns. Following this thermalization step, the ignition of the foil was produced by heating one edge of the sample. The atoms with coordinates $x < 50$ nm were integrated for 0.08 ns into the canonical ensemble (NVT) to reach the ignition temperature $T_{\mathrm{ig}} = 1200$ K,

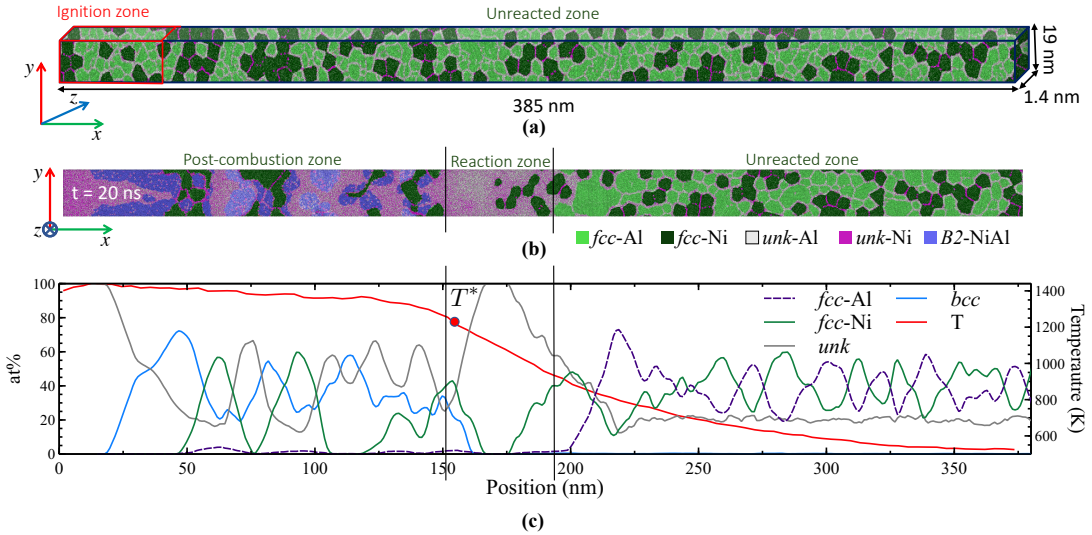

FIG. 1. (a) Schematic representation of the initial state of the sample A with 320 grains. (b) Snapshot of the system at t =20 ns. (c) Quantitative structure analysis and temperature profile at t = 20 ns. The dot indicates T^*, the maximum temperature gradient dT/dx at $t = 20$ ns.

TABLE I. Characteristics of simulated systems.

System	$L_x \times L_y \times L_z (nm)$	mean grain size (nm)	N_{Ni}	N_{Al}
480 × 3.5 nm	334.4 × 16.7 × 1.4	3.5	277724	257034
480 × 3.5 nm #A	334.4 × 16.7 × 1.4	3.5	181746	322017
480 × 3.5 nm #B	334.4 × 16.7 × 1.4	3.5	181746	322017
320 × 5 nm #A	390.0 × 19.5 × 1.4	5.1	368881	370679
320 × 5 nm #B	390.0 × 19.5 × 1.4	5.1	368881	370679
240 × 7.5 nm	506.6 × 25.3 × 1.4	7.7	647729	627622
RMNF $H = 7.25$ nm	420 × 14.50 × 1.4		326400	305466
RMNF $H = 9.25$ nm	420 × 18.50 × 1.4		403200	386694
RMNF $H = 13.7$ nm	420 × 27.40 × 1.4		595200	587202

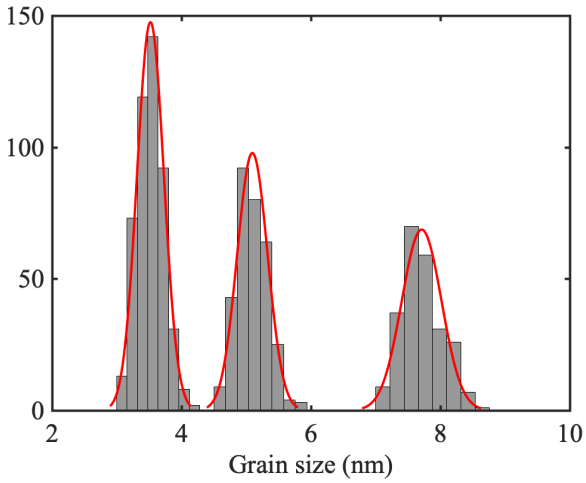

FIG. 2. Histogram of average grain sizes for the polycristalline systems with grains of 3.5 nm, 5 nm, and 7.5 nm.

while all other atoms evolve in the microcanonical ensemble (NVE). After this stage, the local thermostat was removed and the system evolved freely within the NVE ensemble. This numerical procedure, where a local heating induces the propagation of the reaction wave, tries to mimic as closely as possible the experimental procedure.

For all MD runs, the equations of motion were integrated with a time-step equal to 2 fs. The damping parameters were 0.2 ps for temperature and 2.0 ps for pressure. The resulting atomic positions were visualized with the open-source software, OVITO[26]. The local environment (i.e. *fcc*, *bcc* or *unknown*/*amorphous*) was determined for each atoms with the adaptive Common Neighbor Analysis (a-CNA)[27]. In the initial configuration depicted in Fig. 1a, each atom was tagged with an indicator referencing its type and local structure.

III. RESULTS AND DISCUSSIONS

Sections III A (front characteristics) and III B (local dynamics) present the results for the system with 320 grains of 5 nm (system *A*). Section III C discusses the influence

of the initial microstructure by using two distributions of 320 grains (systems *A* and *B*). Section III D compares the combustion modes for CR-nanofoils and RMNFs and evaluates the influence of grain size.

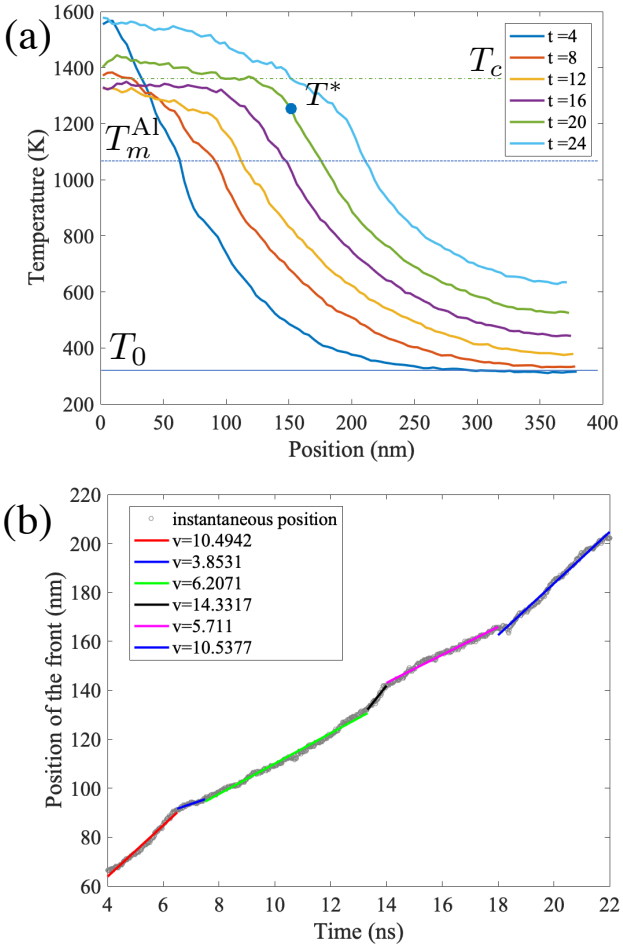

FIG. 3. (a) Temperature profiles in the system A with 320 grains. The horizontal lines indicate: T_0, the initial temperature; T_m^{Al}, the melting temperature of Al; T_c, the combustion temperature at $t = 20$ ns. The dot indicates T^*, the maximum temperature gradient dT/dx at $t = 20$ ns. The temperature profiles are plotted every 4 ns. (b) Front position as a function of time. The position of the front is where the temperature is 1000 K. Velocity units in m/s.

A. Front characteristics

After initiation, the thermal wave propagated across the foil without any further energy supply. The temperature profile was characterized by a broad reaction zone characteristic of solid combustion[28]. The inflection point of the temperature profile, T^*, delineated a zone mainly dominated by conduction ($T < T^*$), and a post-combustion zone ($T > T^*$).

As an example, the snapshot corresponding to the temperature profile at 20 ns is shown in Fig. 1b. Figure 1c gives the at% of atoms for each configuration (*fcc*, *bcc*, and *unknown*) following the a-CNA, together with the temperature profile along the sample. Several regions can be identified in the snapshot. On the right, where the temperature is below the melting point of Al, both metals remain solid (fcc-Al and fcc-Ni). This region corresponds to unreacted material. On the left, the temperature is higher than the representative temperature, T^*. The microstructure is complex: a liquid solution of Ni and Al, and unreacted fcc-Ni grains surrounded by $B2$-NiAl. To the right of the center, grains of fcc-Ni are embedded in a liquid alloy $(\text{Ni+Al})_{\text{liq}}$. The central region is the reaction zone, marked by the melting of Al to the right, and a large number of *unk*-atoms to the left. The melting of Al is the first transformation to occur, followed by the progressive dissolution of Ni in liquid Al. The large amount of heat delivered by exothermic dissolution sustains the self-propagation of the reactive front. Conduction is the only process that heats the unreacted region. A secondary reactive process associated with the crystallization of $B2$-NiAl takes place in the post-combustion zone.

Propagating velocity is a basic characteristic of SHS waves. Figure 3a represents the temperature profiles along the sample at different times. The position of the front, defined here as the position corresponding to a given temperature ($T = 1000$ K), was plotted as a function of time (Fig. 3b). It is noteworthy that the dependence is piecewise linear, with a significant departure from a stationary combustion regime. The velocity shifts from ~ 4 m/s to ~ 10 m/s during propagation. In the absence of heat loss, heating by conduction was observed at the right side of the sample (see Fig. 3a). The width

of the conduction zone can be estimated as $\Delta x = \kappa/v$, where the thermal diffusivity, $\kappa = 4.71\,10^{-6}$ m^2/s, is evaluated at 300 K[21]. For the range of velocities measured, the preheated zone, $\Delta x(T_0 = 300\,\mathrm{K}) = 680$ nm, exceeds the total length of the sample. For larger t values ($t > 22ns$), as the right side of the sample heats up, the reactive front accelerates. In order to avoid this drawback, the data corresponding to these larger t values were not included in further analysis.

B. Local dynamics

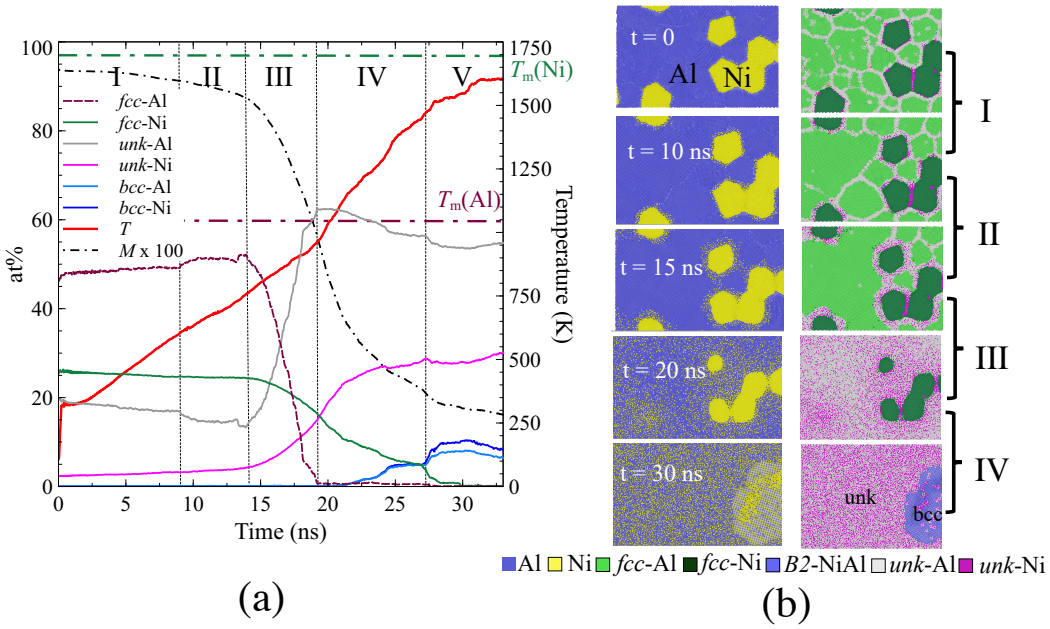

FIG. 4. (a) Structure analysis in a slice of 30 nm, around $x = 180$ nm, in the system A with 320 grains. (b) Snapshots of the slice at different times.

A representative slice was used to analyze local dynamics. Figure 4a shows the evolution of local quantities and temperature, T. The local structure can be depicted in terms of the atomic percentage of atoms in their local environment (*fcc*, *bcc* or *unknown*). Representative snapshots are given in Fig. 4b. A comparative study of

phase transformations and temperature evolution allowed us to identify five stages:

I. The temperature increases because of heating by conduction. No transformation is noted.

II. During stage II, the fraction of *fcc*-Al slightly increases. Grain boundaries between *fcc*-Al grains disappeared. Grain coarsening was observed: small neighboring grains were rearranged into a larger grain.

III. The fraction of *unk*-Al increases as all *fcc*-Al become amorphous. At the end of this stage, there are no more *fcc*-Al atoms. Half of the *fcc*-Ni atoms become *unk*-Ni, due to the dissolution of Ni atoms into the amorphous phase. The temperature T reaches the Al melting point, $T_m^{\mathrm{Al}} = 1055$ K[21].

IV. The fraction of *unk*-Al decreases while the fraction of *unk*-Ni continues to increase. The fraction of *bcc*-atoms increases, together with temperature. These indicators point to nucleation and the growth of a new phase, *B2*-NiAl. The temperature during stage IV remains below the melting temperature of the intermetallic compound ($T_m^{\mathrm{NiAl}} = 1850$ K[21]).

V. A slight dissolution of *B2*-NiAl grains is observed.

In addition to phase transformations (such as melting and *B*2 formation), it is important to track the mixing that is the main process responsible for heat release. Two indicators were introduced in order to track mixing: a local mixing parameter, γ, associated with each atom, and a "mesoscopic" mixing parameter, M, corresponding to a spherical region (with a radius larger than 3 Å, but less than the volume of the whole system). The mixing parameter, M, associated with a slice is defined for an equiatomic system[21]:

$$M = \frac{4}{N_{\mathrm{slice}}} \sum_{\ell=1}^{N_{\mathrm{slice}}} (n_\ell - 0.5)^2 \tag{1}$$

where N_{slice} is the number of atoms in the slice, and n_ℓ is the local mole fraction of Ni in a sphere of 3 Å radius around the ℓ-atom. The mixing parameter has two limits: $M = 0$,

for a homogeneous equiatomic alloy, and $M = 1$, for totally separated unmixed Ni or Al. The mixing parameter was calculated for the slice in the x-direction, $x = 180 \pm 15$ nm (Fig. 4a). The decrease in the mixing parameter actually starts during stage III, with the amorphization of Al atoms, and the progressive dissolution of Ni atoms in Al grains. During stage IV, M further decreases, with the amorphization of Ni grains, and finally reaches a value of 0.2, indicating that the liquid alloy is not perfectly homogeneous.

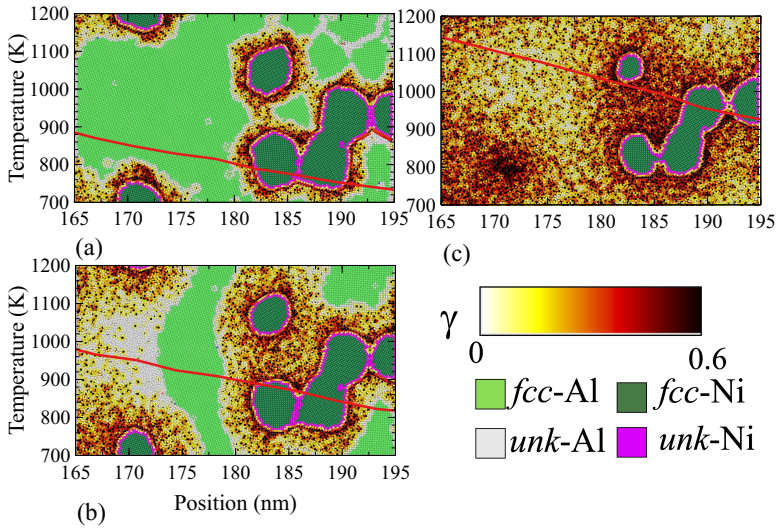

FIG. 5. Snapshots of a slice (as in Fig. 4) at different times: (a) $t = 15$ ns, (b) $t = 17.5$ ns, (c) $t = 20$ ns. Atoms are colored according to their local environment, if their local mixing parameter $\gamma = 0$. In the case, $\gamma \neq 0$, atoms are colored according to the level of mixing. The temperature profile along the slice is plotted in red. (For interpretation of the references to colour in this figure, the reader is referred to the online version of this article.)

The local mixing parameter of atom ℓ, γ, is defined as the number of dissimilar nearest neighbors, divided by the total number of nearest neighbors, in a sphere of radius 3 Å around the atom ℓ. In the case of *B2*-NiAl, one Al atom has 8 Ni atoms as nearest neighbors, and 6 Al atoms in a sphere of radius 3 Å, with $\gamma = 0.57$. Pure Al (or Ni) is characterized by $\gamma = 0$. Figure 5 shows snapshots of the slice 180 ± 15 nm in the x-direction, with the corresponding temperature profile, at different times.

At $t = 10$ ns (Fig. 5a), the temperature is lower than the Al melting point. However, Ni atoms started to dissolve in the grain boundaries between Ni and Al grains, mainly composed of amorphous Al atoms. At $t = 17.5$ ns, the temperature increased through conduction, but remained lower than the bulk melting temperature of Al. Small Al grains surrounding Ni grains lost their fcc-structure and Ni atoms diffused into them. The large Al grain (on the left of Fig. 5b) amorphized gradually, following the thermal gradient. We observed the progressive dissolution of Ni in the Al amorphous region. The mixing is more pronounced around Ni grains. At $t = 20$ ns, the mean temperature is about $T_m(\mathrm{Al})$. All Al atoms have lost their fcc-structure and small Ni grains have disappeared. The progressive dissolution of Ni in Al is indicated by the γ-gradient. The Ni-Ni grain boundaries contain amorphous Ni atoms.

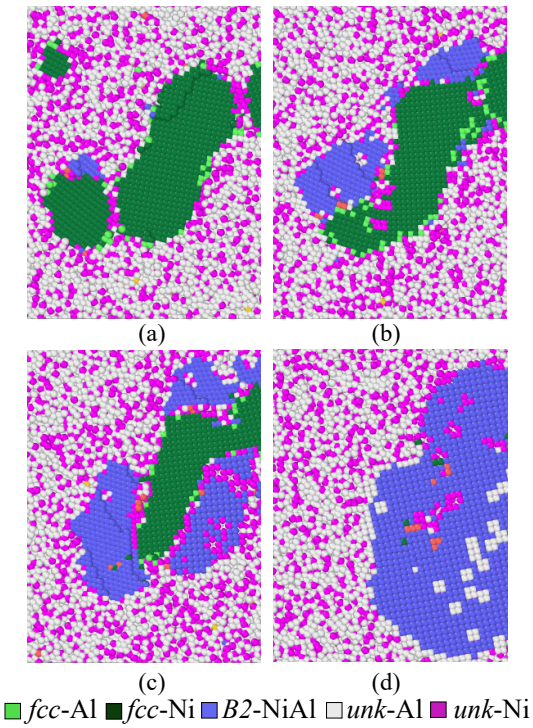

FIG. 6. Crystallization of the *B2*-NiAl phase in the system A with 320 grains. Snapshots at $t = 20.85$ ns (a); $t = 23.10$ ns (b); $t = 24.65$ ns (c); $t = 30$ ns (d).

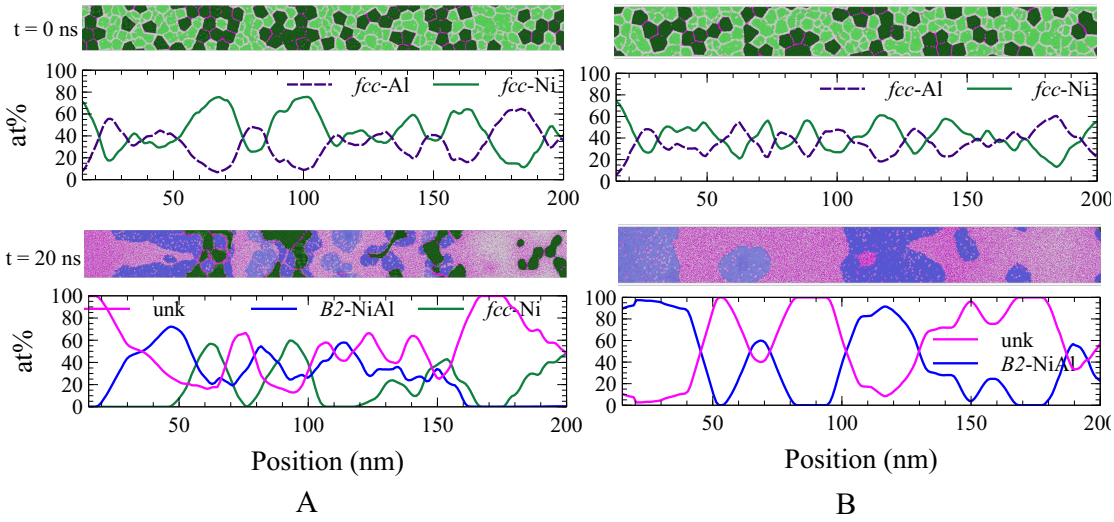

FIG. 7. Two different initial microstructures, A and B, for the system with 320 grains of 5 nm. Snapshots of the systems at t = 0 ns and t = 20 ns, from $x = 0$ nm to $x = 200$ nm (half system), and corresponding structure analysis.

The crystallization of *B2*-NiAl is depicted in Fig. 6. The *B2*-NiAl grains are formed during propagation. After the passage of the dissolution front, the local temperature is still lower than the melting temperature of the intermetallic $T_m(\text{NiAl}) = 1850$ K. Such undercooling conditions are suitable for the rapid solidification of the new phase. As shown in Fig. 6a, *B2*-NiAl grains nucleate at the interface between the liquid solution and solid *fcc*-Ni grains. In a few nanoseconds (Fig. 6b), several nuclei appear, while smaller Ni grains dissolved. Vacancies created during Ni dissolution are occupied by Al atoms. The remaining Ni grain is progressively surrounded by *B2*-NiAl, as the dissolution of Ni into liquid continues (Fig. 6c). Ten nanoseconds after nucleation, small *B2* -NiAl grains coalesce, forming a larger grain that continues to grow (Fig. 6d).

C. Influence of the initial microstructure

Two systems with 320 grains, A and B, were used to investigate the role of the initial microstructure on the front features and final product. The only difference between A and B is the distribution of Al and Ni grains along the sample at $t = 0$ ns, as shown in Fig. 7. In the sample A, regions filled with Ni grains alternate with regions filled with Al grains. Locally, there may be an excess of Ni (or Al). In sample B, the local at.% of Ni and Al fluctuates around 50%. Figure 7 shows the structure of the post-combustion zone after the passage of the reactive front, at $t = 20$ ns. The difference between the two samples is striking. In sample A, some thin solid layers of remaining Ni are embedded in $B2$-NiAl grains. In sample B, large $B2$-NiAl grains coexist with Ni+Al liquid solution.

During propagation, solid Ni progressively dissolves in liquid Al. The Ni and Al atoms mix. Heat is released and an equiatomic liquid solution is formed at a temperature ($T < 1600$ K) below the melting temperature of $B2$-NiAl. The liquid solution thus corresponds to the undercooled NiAl compound, and conditions for the solidification of the intermetallic compound are fulfilled. As described in Section III B, crystallization occurs by heterogeneous nucleation around solid Ni grains. If the crystallization rate is faster than the dissolution rate, which is limited by the solubility of Ni into Al, Ni dissolution may stop. This is actually observed in sample A, in which the distribution of Ni and Al is not uniform along the sample.

Temperature profiles corresponding to sample B are shown in Fig. 8. A plateau is observed in the combustion temperature, T_c, at around 1750 K. By contrast, in sample A (see Fig. 3a), the combustion temperature continuously increased from 1300 K to 1600 K during propagation. This is because $B2$-NiAl is formed during propagation in sample B and after propagation in sample A. In sample B, the reactive front is the superposition of two fronts: the exothermic dissolution front, and the $B2$-NiAl crystallization front, both moving forward at the same speed. In sample A, $B2$-NiAl crystallization takes place in the post-combustion zone. In both A and B, the reactive front propagation is unsteady (see Fig. 3b). As shown in Fig. 9a, the speed is constant over short time

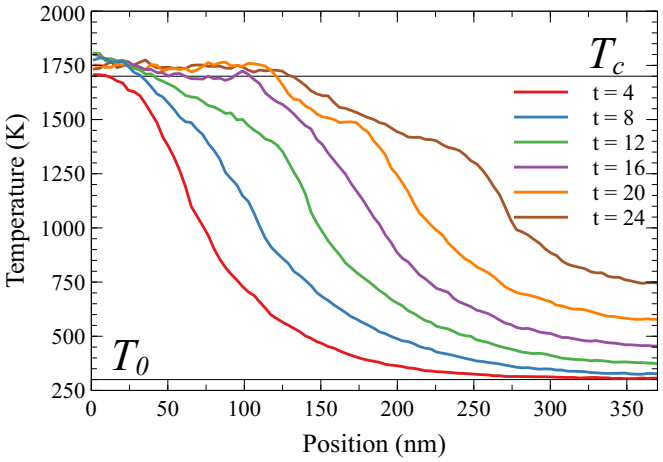

FIG. 8. Temperature profiles in sample B with 320 grains. The horizontal lines indicate the initial temperature T_0, and the combustion temperature T_c at $t = 16$ ns.

periods (sectors), but with significant variability. The weighted arithmetic mean velocity can be estimated as

$$u = \frac{\sum_{\ell=1}^{N_t} u_\ell \times \Delta t_\ell}{\sum_{\ell}^{N_t} \Delta t_\ell} \tag{2}$$

where u_ℓ is the constant speed over a given sector, Δt_ℓ, and N_t is the number of sectors. In sample B, Δt_ℓ are similar whatever the u_ℓ value. By contrast, in sample A, the sectors Δt_ℓ vary considerably in length. The number of sectors, N_t, is larger in B than in A. The mean velocity, u, is also different ($u_A = 7.83$ m/s, and $u_B = 9.48$ m/s), proving that front characteristics are dependent on the initial microstructure.

The self-propagating front is triggered and sustained by heat release due to exothermic dissolution and $B2$-NiAl crystallization. Figure 9b compares the overall number (at.%) of fcc-, bcc- and *unk*-atoms as a function of time. During propagation (up to 24 ns), the two elemental processes are in advance in sample B. The rapid decrease in fcc-atoms is accompanied with amorphization and direct crystallization of $B2$-NiAl. In sample A, the slower decrease in fcc-atoms is mainly related to amorphization, with intermixing of Ni and Al atoms. This fact explains the excess of heat release observed in sample B. After 24 ns, the temperature becomes more or less uniform, and we can

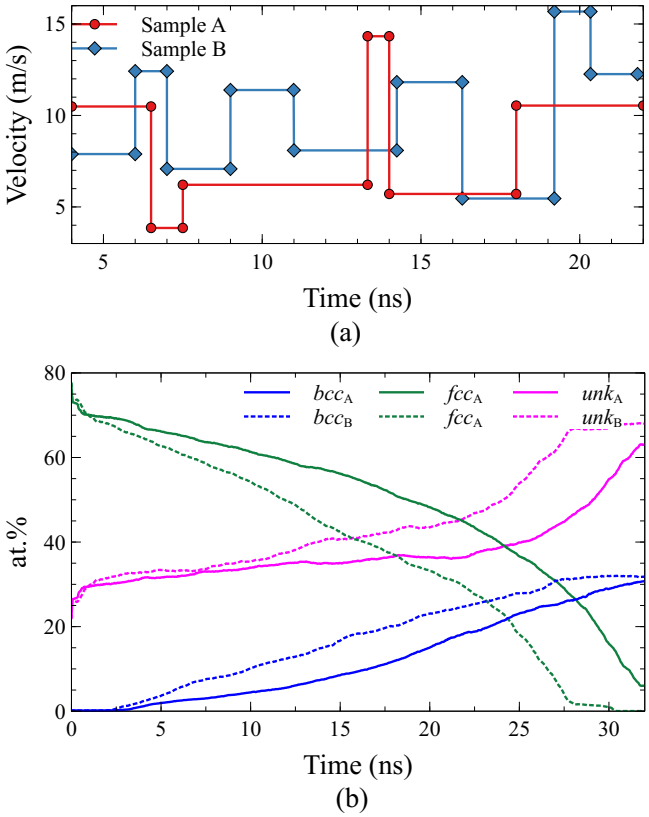

FIG. 9. (a) Velocity u_ℓ measured in samples with 320 grains (#*A* and #*B*) as a function of time. (b) Overall number of fcc-, *bcc*- and *unk*-atoms as a function of time in samples *A* and *B*. (b) Overall number (at.%) of fcc-, *bcc*- and *unk*-atoms as a function of time in samples *A* and *B*.

no longer speak of a propagative mode. During this final stage, sample *B* remains in advance, in both amorphization and *B*2-NiAl formation. At the end, both systems contain the same amount of intermetallic compound, but sample *A* still retains a few fcc-atoms (clusters of fcc-Ni), while sample *B* only contains *bcc*- and *unk*-atoms.

The heat released by the two elemental processes can be further investigated on the basis of the potential energy/atom, E_0. For this purpose, the evolution of a slice that mainly contains Al atoms at $t = 0$ ns is plotted in Fig. 10. At $t = 13$ ns, the temperature is 910 K and progressive amorphization of Al occurs. Slightly later, at $t = 13.5$ ns, the

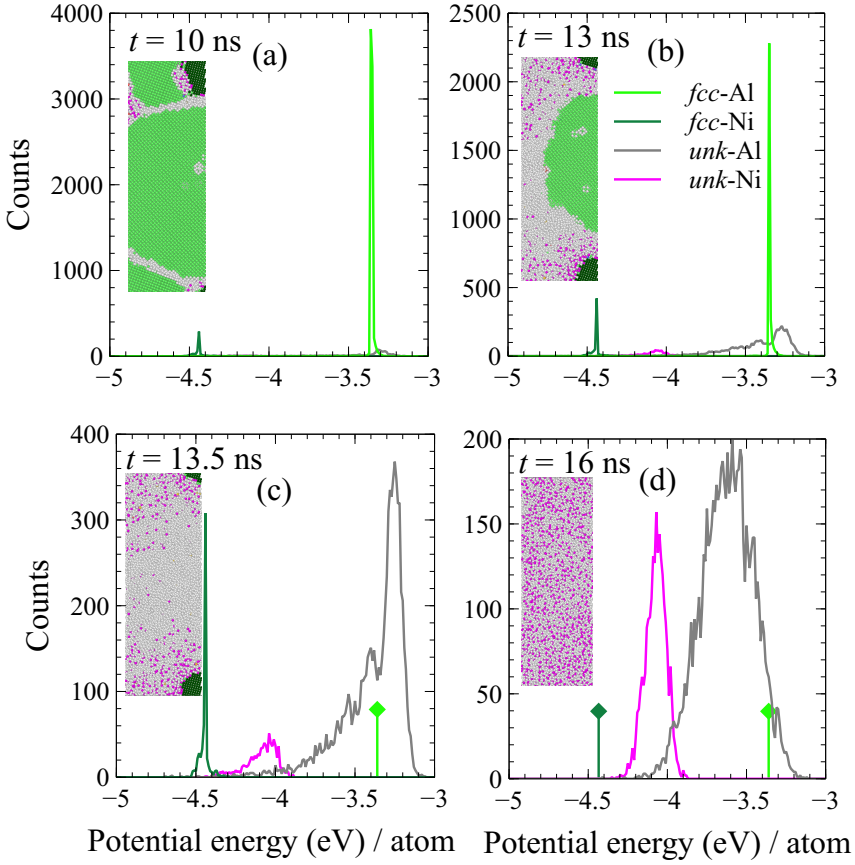

FIG. 10. Histograms of potential energy/atom in a slice, at times $t = 10$ ns, $t = 13$ ns, $t = 13.5$ ns, and $t = 16$ ns. The corresponding snapshot is represented as an insert. Vertical lines indicate the values of the potential energy per atom for pure Al and pure Ni.

temperature reaches 943 K, all fcc-Al have disappeared, and Ni-atoms start to dissolve. The distribution of potential energy/atom expands, with a maximum value higher than the value of pure Al, $E_0(fcc-\mathrm{Al})$ = -3.36 eV/atom. At $t = 16$ ns, incoming Ni atoms from adjacent slices dissolve. The temperature rises to 1273 K through exothermic mixing and conduction. The Al distribution peak shifts to a lower value, while the Ni distribution peak is higher than the value of pure Ni, $E_0(fcc-\mathrm{Ni})$ = -4.45 eV/atom. In the case of exothermic dissolution and mixing,

$$\mathrm{Ni_s} + \mathrm{Al_s} \rightarrow \mathrm{NiAl_{liq}} \tag{3}$$

the balance reads

$$\begin{aligned} &E_0(fcc{-}\mathrm{Ni}) + E_0(fcc{-}\mathrm{Al}) \\ &= E_0(unk{-}\mathrm{Ni}) + E_0(unk{-}\mathrm{Al}) + Q_{\mathrm{diss}} \end{aligned} \tag{4}$$

with $Q_{\mathrm{diss}} = 0.15$ eV/atom where $E_0(\mathrm{unk})$ is evaluated as the histogram peak in Fig. 10d.

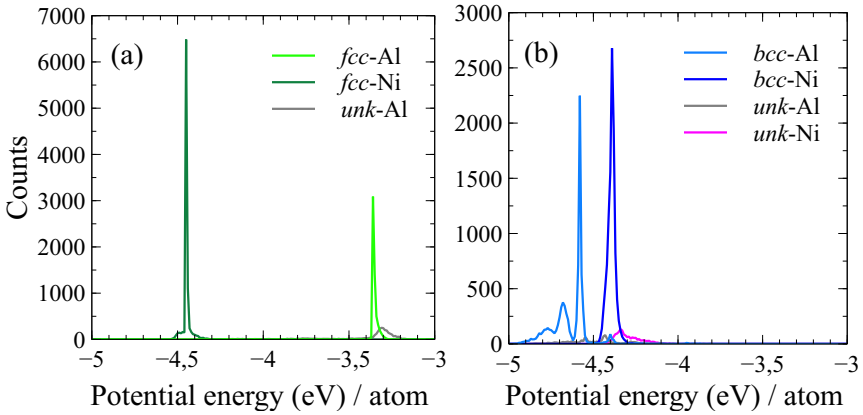

FIG. 11. Histograms of potential energy/atom in a slice where $B2$-NiAl is formed at times $t = 0$ ns, and $t = 30$ ns.

We then considered another slice that was completed transformed into $B2$-NiAl after the passage of the reactive front (Fig. 11). The exothermic reaction between nickel and aluminum, gives rise to the formation of the compound NiAl,

$$\mathrm{Ni_s} + \mathrm{Al_s} \rightarrow \mathrm{NiAl_s} \tag{5}$$

Under the strong hypothesis that the Ni atom keeps its potential energy until the reaction takes place, the energy balance expressed in terms of potential energy per atom reads

$$\frac{1}{2}[E_0(fcc{-}\mathrm{Ni}) + E_0(fcc{-}\mathrm{Al})] = E_0(\mathrm{NiAl}) + Q_{\mathrm{reac}} \tag{6}$$

where $Q_{\mathrm{reac}} = 0.573$ eV/atom is the excess of energy liberated by atomic rearrangement. The potential energy, $E_0(\mathrm{NiAl})$, was estimated using the histograms. The amount

of heat, Q_{reac}, released through the formation of $B2$-NiAl is thus greater than the heat release associated with the exothermic mixing, Q_{diss}. This results explain why crystallization promotes a higher combustion temperature (sample B compared to sample A).

D. Combustion mode

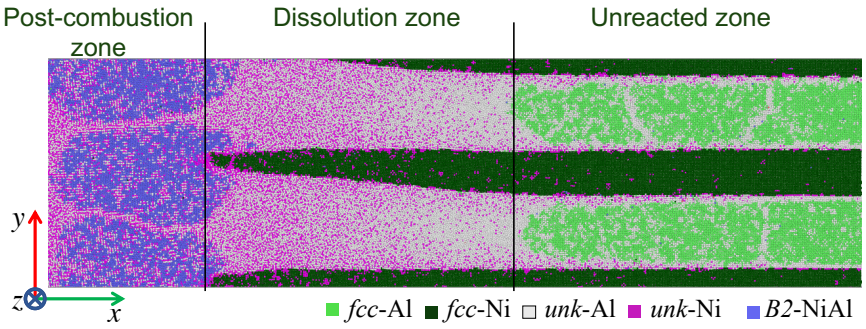

FIG. 12. Snapshot of a lamellar system with equimolar stoichiometry ($n_{\text{Ni}} = 0.5$) and bilayer thickness $H = 13.5$ nm. Only a slice of 100 nm around the reaction zone is represented.

Lamellar systems with constant bilayer thickness are among the most thoroughly studied nanometric heterogeneous systems. In the RMNF system presented here, the combustion front propagates parallel to the layers of reactants. In the case of Ni-Al nanofoils, different reactive regimes were described according to their stoichiometry and initial temperature[29]. For low initial temperature, $T_0 = 300$ K, a specific heterogeneous reaction mechanism, *rapid crystallization from melt*, was observed, as shown in Fig. 12. The unreacted zone is characterized by constant layer thickness. The reactive dissolution zone zigzags, through the progressive dissolution of Ni in the liquid Al. The final product is a solution of Ni and Al, plus $B2$-NiAl. The nuclei appear at the tip of the solid Ni fingers, and grow in the undercooled liquid solution, Ni + Al. This system can be considered as an "ideal" counterpart to CR-nanofoils where all Ni (Al) grains are aligned. The reaction zone starts with the melting of Al and ends with the complete

dissolution of Ni. The exothermic process associated with dissolution and intermixing sustains front propagation. The width of the reaction zone, where the dissolution of Ni takes place, corresponds to the region over which the temperature increases from the melting point of Al to the combustion temperature. The reactive front that crosses the layers is planar, and its velocity is constant. This behavior is referred to as a "quasi-homogeneous" mode of propagation, corresponding to a steady planar propagation.

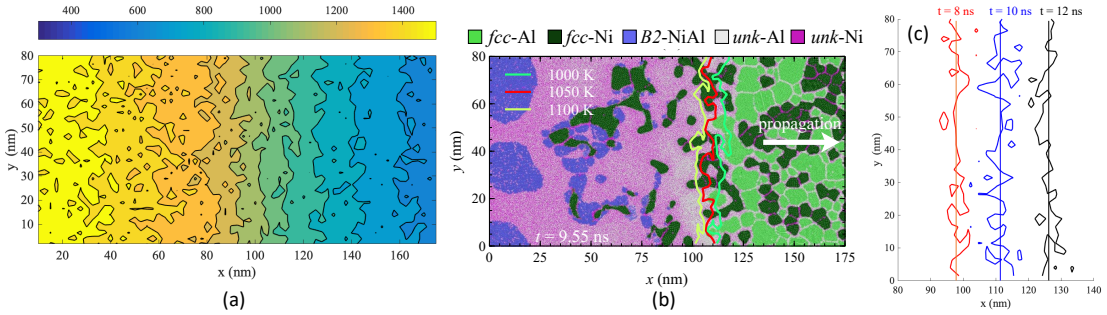

FIG. 13. Wide system with randomly distributed 5 nm grains of Ni and Al. (a) Contour plot of the instantaneous temperature field in a section (x,y). Each line corresponds to a temperature from $T = 300$ K to $T = 1500$ K, in 100 K steps. A slice in the x-direction (0-175 nm), $t = 9.55$ ns. (b) Corresponding snapshot. (c) Front propagation. Contour line corresponds to 1050 K. The straight line indicates the mean position along the y-direction. Slices in the x-direction (80-140 nm), at times $t = 8$ ns, $t = 10$ ns and $t = 12$ ns.

Next, we re-examined the system with randomly mixed grains. The system in Fig. 13 has the same characteristics as those presented in the previous sections, but is 4 times wider in the y-direction. Figures 13a and 13b give two representations of the same system at a given time while the front was propagating along the sample. Fig. 13a is a coarse-grained picture of the local temperature field. Fig. 13b depicts the snapshot of the system with superimposed temperature contours at temperatures values around the melting point of Al. The contour plots of the temperature field are depicted in a slice in the x-direction, from $x = 0$ to $x = 175$ nm. The local temperature was estimated in a mesh grid with 2.5 x 2.5 nm cells. This corresponds to *in situ* observation of rapid

processes occurring at microscopic level, as obtained by digital high-speed microscopic video recording[30]. The shape of the temperature profile in the direction perpendicular to front propagation (y-direction) is actually not planar but rather tortuous. Locally, the temperature is either higher, reflecting increased reactivity, or lower, reflecting decreased reactivity. These irregularities are not the same in successive contour lines, indicating the possibility of front activity in a lateral direction, associated with heat transport and the creation of new hot spots. This unsteady propagation mode was observed experimentally, with the formation of reaction bands that grow and spread normal to the propagation direction, and parallel to the reaction front[11]. In order to find the relationship between the microstructure of the reaction media and the combustion wave, we plotted the temperature contours on the corresponding snapshot (Fig. 13b). Small fcc-Al grains surrounded by fcc-Ni melted below the Al melting point (1055 K) and became active sites for exothermic dissolution, while larger Al-grains remained solid. The contour lines corresponding to 1050 K at different times are plotted in Fig. 13c. Great dispersion is observed around the mean value in the y-direction. These fluctuations indicate great temperature variability during propagation. As shown in Fig.13a, the contour line for temperatures close to the combustion temperature ($T \geq 1400$ K) shows distortions and hot spots in the front. This pattern is related to the random crystallization and consecutive growth of the $B2$-NiAl phase during post-combustion. The random character of crystallization is associated with the underlying microstructure because of heterogeneous nucleation of the $B2$-NiAl phase on the randomly distributed fcc-Ni grains.

A rough estimate of the characteristic time for heat relaxation is $\tau_{\text{heat}} = \kappa/\ell^2 = 0.0256$ ns, where $\kappa = 0.975 \times 10^{-6}$ m/s^2 is the heat diffusivity of Al at melting point[24] and $\ell = 5$ nm is a characteristic length scale (here, grain size). If we assume that the reactive dissolution is limited by diffusion of Ni in liquid Al, the characteristic diffusion time is $\tau_{\text{reac}} = D/\ell^2 = 5.68$ ns $\gg \tau_{\text{heat}}$, where D is evaluated at T_{m} (Al)[18]. Since heat relaxation is very efficient, the heterogeneous character of the front is directly related to

TABLE II. Front characteristics.

System	at.% Ni	regime	u	T_c [a]
480 × 3.5 nm	51.9 %	nearly-steady	14.9 m/s	1500-1700 K
480 × 3.5 nm #A	36%	unsteady	6.35 m/s	1300 K
480 × 3.5 nm #B	36%	unsteady	7 m/s	1300 K
320 × 5 nm #A	50%	unsteady	7.83 m/s [b]	1350-1600 K
320 × 5 nm #B	50%	unsteady	9.48 m/s [b]	1750 K
240 × 7.5 nm	50.8%	arrested front		
RMNF $H = 7.25$ nm	51.6 %	steady	14.2 m/s	1700 K
RMNF $H = 9.25$ nm	51 %	steady	11.95 m/s	1570-1750 K
RMNF $H = 13.7$ nm	50.3 %	arrested front		

[a] The combustion temperature is evaluated during the propagation regime.

[b] Weighted arithmetic mean velocity (2).

local reactivity in the system.

We evaluated systems with different grain sizes. Front characteristics (velocity, combustion regime, and combustion temperature) are reported in Table II. An equiatomic system composed of 480 randomly distributed grains, with a radius of 3.5 nm, was characterized by a quasi-steady combustion regime. Propagation was almost stationary, with small deviations around the linear dependence of the front position as a function of time. Front velocity was much higher than in systems with 5 nm grains. When the initial system contained an excess of Al, unsteady combustion was observed, with lower velocity and combustion temperature. Less $B2$-NiAl was formed, proving that $B2$-NiAl formation plays an important role in front propagation, by adding a significant heat source to the heat delivered by exothermic dissolution.

The sample composed of grains with a radius of 7.5 nm or larger, prepared at 300 K, showed no self-sustaining propagation of the reactive wave. After ignition, the reaction

began with the melting of Al, the exothermic dissolution of Ni in Al, and the formation of NiAl grains. However, the heat delivered by these processes was not sufficient for self-propagation. The front arrested after a few nanoseconds.

For comparison, Table II gives the front characteristics of RMNFs with constant bilayer thickness. Systems with 3.5 nm and 5 nm grains can be compared to RMNFs with $H = 7$ and 10 nm. In the case of RMNFs with $H = 7.25$ and 9.25 nm, the front propagated in a steady regime. After nucleation of $B2$-NiAl at the tips of solid Ni fingers, $B2$-NiAl grains grew in the liquid solution and expanded into larger regions. For greater bilayer thickness, $H = 13.7$ nm (see Fig. 12), the reaction began but the heat delivered was not sufficient to sustain propagation, as was the case for samples with randomly distributed grains with a radius of 7.5 nm.

IV. CONCLUSIONS

Peculiarities of front propagation were investigated in samples composed of randomly distributed grains with an initial temperature, $T_0 = 300$ K:

- The heat that sustains the self-propagating front is delivered by the exothermic dissolution of Ni in liquid Al, and by direct crystallization of $B2$-NiAl from the undercooled liquid Ni+Al solution.

- The amorphization and melting of the Al phase takes place below the melting temperature of the bulk material. This is more pronounced for Al grains surrounded by Ni grains. Heating by conduction led to the coarsening of contiguous Al grains. Thus, local melting directly depends on the initial configuration of the system.

- In the initial system, most amorphous atoms are Al atoms. Dissolution of Ni starts at amorphous grain boundaries.

- A departure from steady combustion occurs as front velocity fluctuates, jumping

between lower and higher values. This effect is less pronounced for small grains. The velocity behavior is directly related to the initial configuration of the sample.

- Propagation is arrested for larger grains ($\geq$ 7.5 nm).

- Due to the finite length of the system, and slow propagation, the heat conduction zone may become as large as the whole system. As a consequence, propagation is often followed by global heating with a rapid reaction (explosion).

Compared to RMNFs with constant bilayer thickness, where the combustion front propagates parallel to the layers, CR-nanofoils with randomly distributed grains show greater complexity in their front characteristics. Propagation is unsteady, with a velocity that directly depends on the initial configuration. The temperature profile in the direction perpendicular to front propagation is irregular, reflecting local chemical activity. The final microstructure also depends on the initial configuration, but the reactivity of CR-nanofoils makes them an interesting alternative, for most applications.

ACKNOWLEDGMENTS

The use of computational facilities at the Computing Center of the University of Bourgogne, PSIUN-CCUB, is gratefully acknowledged.

DATA AVAILABILITY

The data that support the findings of this study are available from the corresponding author upon reasonable request.

REFERENCES

[1]G.M. Fritz, H. Joress, T. Weihs, Combust Flame. 158, 1084-88 (2011)

[2]Q. Zeng, T. Wang, M. Li, Y. Ren, Appl. Phys. Lett. 115, 093102-5 (2019)

[3]B. Rheingans, I. Spies, A. Schumacher, S. Knappmann, R. Furrer, L.P.H. Jeurgens, J. Janczak-Rusch, Appl. Sci. 9, 262 (2019)

[4]A.S. Rogachev, S.G. Vadchenko, A.A. Nepapushev, S.A. Rogachev, Y.B. Scheck, A. Mukasyan, Adv. Eng. Mater. 20, 1701044 (2018)

[5]T.W. Barbee and T. Weihs, U.S. Patent N 5538795, July 23 (1996)

[6]S. Danzi, V. Schnabel, X. Zhao, J. Käch, R. Sponelak, Appl. Phys. Lett. 114, 183102 (2019)

[7]A. Sáenz-Trevizo, A.M. Hodge, Nanotechnology 31, 292002 (2020)

[8]T.P. Weihs, in: D.A. Glocker, S.I. Shah (Eds.), "Handbook of Thin Film Process Technology", IOP Publishing, Bristol (1998)

[9]D.P. Adams, Thin Solid Films 576, 98-128 (2015).

[10]H. Sieber, J.S. Park, J. Weissmüller and J.H. Perepezko, Acta Mater. 49 (2001) 1139-1151.

[11]A.K. Stover, N.M. Krywopusk, G.M. Fritz, S.C. Barron, J.D. Gibbins, T.P. Weihs, J Mater Sci. 48, 5917-5929 (2013).

[12]F. Baras, V. Turlo, O. Politano, A.S. Rogachev, A.S. Mukasyan 2018, Adv. Eng. Mater. 20, 1800091 (2018).

[13]B. Witbeck, J. Sink, D.E. Spearot J. Appl. Phys. 124, 045105 (2018).

[14]B. Witbeck, D.E. Spearot, J. Mater. Res. 34, 2229-2238 (2019).

[15]B. Witbeck, D.E. Spearot, J. Appl. Phys. 127, 125111-11 (2020).

[16]F. Baras, O. Politano, Phys. Rev B 84, 024113 (2011).

[17]O. Politano, F. Baras, J. Alloy Compd. 652, 25-29 (2015).

[18]V. Turlo, O. Politano, F. Baras, Acta Mater 99, 363-372 (2015).

[19]V. Turlo, O. Politano, F. Baras, Acta Mater 120, 189-204 (2016)

[20]A.S. Rogachev, S.G. Vadchenko, F. Baras, O. Politano, S. Rouvimov, N.V. Sachkova, M.D. Grapes, T.P. Weihs, A.S. Mukasyan, Combust. Flame 166, 158-169 (2016).

[21]V. Turlo, O. Politano and F. Baras, J. Appl. Phys. 121, 055304-15 (2017).

[22]see http://lammps.sandia.gov/; S. Plimpton, J. Comp. Phys. 117, 1 (1995).

[23]G. Purja Pun, Y. Mishin, Phil. Mag. 89, 3245-3267 (2009).

[24]V.Turlo, F. Baras and O. Politano, Modelling Simul. Mater. Sci. Eng. 25, 064002 (2017).

[25]A. Perron, S. Garruchet, O. Politano, G. Aral, V. Vignal, J. Phys. Chem. Solids. 71, 119-124 (2010).

[26]A. Stukowski, Model. Simul. Mater. Sci. Eng. 18, 015012 (2010)

[27]A. Stukowski, Modelling Simul. Mater. Sci. Eng. 20, 045021 (2012)

[28]I.P. Borovinskaya, A.A. Gromov, E.A. Levachov, Y.M. Maksimov, A.S. Mukasyan, A.S. Rogachev, eds., "Concise encyclopedia of self-propagating high-temperature synthesis", Elsevier (2017).

[29]V. Turlo, O. Politano and F. Baras, J. Alloys Compds. 708, 989-998 (2017).

[30]A. S. Mukasyan, A. S. Rogachev, M. Mercedes, A. Varma, Chem. Eng. Sc. 59, 5099-5105 (2004).